Chemical Engineering Science 136 (2015) 50–61

Contents lists available at ScienceDirect

Chemical Engineering Science

journal homepage: www.elsevier.com/locate/ces

Multiscale modeling and operation of PECVD of thin film solar cells

Marquis Crose [a], Joseph Sang-Il Kwon [a], Michael Nayhouse [a], Dong Ni [c], Panagiotis D. Christofides [b,a,*]

[a] Department of Chemical and Biomolecular Engineering, University of California, Los Angeles, CA 90095, USA
[b] Department of Electrical Engineering, University of California, Los Angeles, CA 90095, USA
[c] Institute of Automation, Chinese Academy of Sciences, Haidian District, Beijing 100190, China

HIGHLIGHTS

- Novel microscopic model of thin film microstructure evolution.
- Multiscale PECVD model accounting for wafer grating.
- Novel operation policy for large-area thin film deposition.
- Uniform film thickness and surface microstructure that optimizes light trapping.

ARTICLE INFO

Article history:
Received 30 August 2014
Received in revised form
15 January 2015
Accepted 23 February 2015
Available online 3 March 2015

Keywords:
Process modeling
Process optimization
Plasma-enhanced chemical vapor deposition
Thin film solar cells
Thin film surface morphology
Thin film thickness

ABSTRACT

This work proposes a multiscale modeling and operation framework for plasma-enhanced chemical vapor deposition (PECVD) of thin film silicon solar cells with uniform thickness and film surface microstructure that optimizes light trapping. Specifically, we focus on a single-wafer parallel-electrode PECVD process with showerhead arrangement and develop a multiscale model capturing both the gas-phase reaction and transport phenomena that lead to the deposition of the thin film across the wafer as well as multiple microscopic models that describe the evolution of the thin film surface microstructure at equispaced, discrete spatial locations across the wafer. While the modeling of chemical reactions and transport-phenomena (both diffusion and convection) in the gas-phase adopts the continuum hypothesis and is based on two-dimensional in space partial differential equations, a novel microscopic model is developed for the *a*-Si:H thin film surface evolution, which accounts for four microscopic processes: physisorption, surface migration, hydrogen abstraction and chemisorption. A hybrid kinetic Monte Carlo (kMC) algorithm is utilized to reduce computational requirements without compromising the accuracy of established chemical models that account for interactions amongst physisorbed radicals, and the microscopic model fidelity is established though calibration with experimentally obtained growth rates and surface morphology data. The results of the multiscale process model indicate that in order to produce a thin film with a diameter of 20 cm and a uniform thickness with surface microstructure that optimizes light trapping: (a) a sinusoidally grated wafer surface should be used in which the grating period and depth should correspond to values that lead to film surface roughness and height–height correlation length that are on the order of visible light wavelength range, and (b) the substrate temperature should be adjusted, along several concentric zones across the substrate, to compensate for a radially non-uniform deposition rate of the film on the wafer owing to gas-phase transport phenomena. Due to the dependence of film growth rate on substrate temperature, the wafer surface is separated into four concentric zones, each with an independent heating element. Extensive simulations demonstrate that the use of appropriate sinusoidal wafer grating and the regulation of substrate temperature provide a viable and effective way for the PECVD of thin film silicon solar cells with uniform thickness and film surface microstructure that optimizes light trapping.

* Corresponding author at: Department of Chemical and Biomolecular Engineering, University of California, Los Angeles, CA 90095, USA. Tel.: +1 310 794 1015; fax: +1 310 206 4107.
E-mail address: pdc@seas.ucla.edu (P.D. Christofides).

http://dx.doi.org/10.1016/j.ces.2015.02.027
0009-2509/

1. Introduction

Plasma enhanced chemical vapor deposition (PECVD) is widely used in the microelectronics and solar cell industries to deposit thin films from a mixture of gas-phase species onto a solid substrate (Kern, 1991). Specifically, in the solar cell industry, PECVD is broadly used in the production of thin film silicon solar cells to deposit amorphous silicon semiconductor layers due to low manufacturing costs via silane recycling (Kreiger et al., 2013), the possibility for extremely low operating temperatures ($\leq 250\ ^{\circ}C$) (Yang et al., 2000), and the desirable dielectric properties of amorphous silicon thin films (Rech and Wagner, 1999). However, even high quality amorphous silicon solar cells suffer from efficiencies (of solar power conversion) that are lower than their crystalline counterparts which has motivated significant efforts to improve other thin film light trapping attributes to increase solar power conversion (Green et al., 2014). In this direction, periodic surface textures have been recently proposed in an effort to increase light scattering on the thin film surface or interface and to obtain photocurrents from *a*-Si:H thin film solar cells competitive with other existing solar cell technologies (Eisele et al., 2001; Heine and Rudolf, 1995; Zeng et al., 2008; Sai et al., 2008). Optical simulations of thin films with periodic surface textures (grown on appropriately grated wafers) have demonstrated up to 35% more photocurrent when compared to traditional, flat interfaces (Campa et al., 2010), particularly when the surface roughness and height–height correlation length are comparable to visible light wavelength length scales. Although photolithographic fabrication techniques allow for the creation of grated wafer substrates (van-Erven et al., 2008), in practice, it is not easy to achieve consistent morphology of the surface of an absorbing layer due to the need to deposit thin films over a large area. Significant non-uniformity in final film thickness and variations in surface morphology may occur due to the consumption of reactants as process gases travel radially across the wafer, leading to radially varying deposition rates (e.g., (Armaou and Christofides, 1999; Stephan et al., 1999; Sansonnens et al., 2003)).

In the context of thin film surface morphology control, several model-based control schemes have been applied to deposition process models with the goal of improving solar cell performance through the achievement of periodic film surface textures (e.g., (Huang et al., 2012a,b)). These models typically rely on kinetic Monte Carlo (kMC) algorithms to simulate deposition processes, focusing on evolution of thin film surface microstructure in nano- to micrometer length scales. The concept of using grated wafers to impart periodic surface textures to thin films has existed for some time (Geis et al., 1979), and over the past three decades extensive efforts have been made in optimizing grating shape for the purposes of light trapping (Campa et al., 2010; Eisele et al., 2001; Heine and Rudolf, 1995; Zeng et al., 2008; Sai et al., 2008). Four parameters define the final shape of textured thin films: periodic shape (e.g., rectangular wave, pyramidal, sinusoidal, etc.), height H, period P, and film thickness τ. Given that film growth is driven by the formation of dangling bonds, surface migration has little effect on the shape of thin films beyond local roughness, and as a result, grated wafers can consistently impart optimized textures to thin films. However, practical applications of the existing modeling and control approaches to deposit thin films with tailored surface textures need to address the fact that the film deposition takes place over a large area, leading to the possibility of non-uniformity in film thickness at the reactor scale. Specifically, non-uniformity in reactant and product gas phase species concentrations is negligible on the scale of a single grating period (on the order of hundreds of nanometers), nullifying the need for spatially controlled film thickness at the nanoscale. However, at the reactor length scale (e.g., a 20 cm wafer is used in this work) consumption of reactants across the wafer surface has been shown to yield growth rate differences greater than 19% (Armaou and Christofides, 1999; Stephan et al., 1999; Sansonnens et al., 2003), prompting the need for reactor scale control.

In addition to film thickness uniformity control, the physics of the gas-phase species and film surface interactions should be carefully modeled in the microscopic film growth model when the film growth takes place in a PECVD process. Specifically, due to the vast number of species introduced by the presence of plasma, microscopic modeling of film growth by PECVD is a challenging task. Often the level of modeling detail must be compromised in lieu of simulation efficiency: for example, Novikov et al. (2009) developed a kMC algorithm capable of simulating films several hundred monolayers thick, however, important surface phenomena such as diffusion (migration) were ignored. Conversely, Pandey et al. (2009) conducted more detailed kMC simulations that included diffusion of surface radicals, and although their results appeared in good agreement with experimental data, their work was limited to a relatively small number of monolayers. A close look in the literature indicates a broad agreement of accounting for microscopic events such as the physisorption, migration, and chemisorption of surface radicals in the modeling of the nanostructure of growing thin films in PECVD.

Motivated by the above considerations, this work proposes a multiscale modeling and operation framework for plasma-enhanced chemical vapor deposition (PECVD) of thin film amorphous silicon solar cells. The interdependence of the gas phase and film growth phenomena means that neither can be ignored; as an example, the film growth rate and roughness are strongly tied to the rate of physisorption of surface radicals, which in turn is governed by the inlet concentration of silane and hydrogen gases. Conversely, hydrogen abstraction from the surface into the gas phase influences the overall concentration of reactive radicals. Given the computational challenge of using a single microscopic model to describe the entire PECVD process behavior, the disparity in scales necessitates the need for a multiscale model capable of capturing both the macro- and microscopic phenomena involved in thin film growth processes. Therefore, a multiscale model is developed capturing both the gas-phase reaction and transport phenomena that lead to the deposition of the thin film across the wafer as well as multiple microscopic models that describe the evolution of the thin film surface microstructure at equispaced, discrete spatial locations across the wafer. While the gas phase model is standard, the microscopic model, describing the *a*-Si:H thin film surface evolution, is computationally efficient and accounts for four microscopic processes: physisorption, surface migration, hydrogen abstraction, and chemisorption. Specifically, a nanoscale hybrid kMC scheme originally developed by Tsalikis et al. (2013) is applied to the growth of silicon films with periodic surface textures in an effort to maintain fidelity to established chemical models while allowing for practical computational requirements. The model considers the two dominant species involved in the growth of amorphous silicon films, H and SiH_3 (Perrin et al., 1998; Gallagher, 1988), and four corresponding surface processes: physisorption from the gas phase, hydrogen abstraction by SiH_3, chemisorption onto dangling bonds, and migration across neighboring, hydrogenated lattice sites. As opposed to traditional kMC formulations, surface migration is handled in a decoupled manner from the other processes allowing for efficient simulations in excess of 1000 monolayers. The results of the multiscale process model indicate that in order to produce a 20 cm thin film of uniform thickness with surface microstructure that optimizes light trapping: (a) a sinusoidally grated wafer surface should be used in which the grating period and depth should correspond to values that lead to film surface roughness and height–height correlation length that are on the order of

visible light wavelength range, and (b) the substrate temperature should be adjusted to compensate for a radially non-uniform deposition rate of the film on the wafer owing to gas-phase transport phenomena. This insight motivates an operation strategy that manipulates substrate temperature to produce thin film silicon solar cells with uniform thickness and film surface microstructure that optimizes light trapping.

The paper is structured as follows: first, the multiscale modeling framework for PECVD will be introduced including a brief description of the macroscale gas phase model and the microscale surface interactions. Next, a detailed description of the lattice implementation and corresponding hybrid kMC scheme are provided. Simulations using a flat lattice demonstrate that the proposed hybrid kMC algorithm reproduces experimentally obtained surface morphologies and growth rates at the nanoscale, and that roughness is limited to a few nanometers. Grating is then applied to the wafer with a period and depth corresponding to values that lead to film surface roughness and height–height correlation length that are on the order of visible light wavelength range. Open-loop simulations also reveal a radially non-uniform deposition rate of the film on the wafer owing to gas-phase transport phenomena. Finally, a scheme using four concentric substrate temperature control zones is proposed to successfully regulate film thickness radially across the wafer surface while producing a desired thin film surface microstructure that is demonstrated to be robust with respect to model uncertainty.

2. PECVD process description and modeling

We consider a PECVD chamber shown in Fig. 1 utilizing two parallel electrodes with a single wafer placed on top of the lower electrode. A showerhead arrangement is employed in this PECVD process to uniformly distribute the influent gas stream consisting of silane and hydrogen throughout the chamber and an RF (radio frequency) power source generates plasma (i.e., chemically reactive mixture of ions, electrons, and radicals) from silane. Thin film growth occurs as radicals are transported to the wafer surface via diffusion and convection where they react to form amorphous silicon (*a*-Si:H). The objective of this process is to deposit a 300 nm thick *a*-Si:H thin film on a wafer with a diameter of 20 cm.

Fig. 1 illustrates the multiscale character of this process and the need to capture both the microscopic surface interactions and growth, as well as the macroscopic gas-phase dynamic material balance. Details of both the macroscopic gas phase model and the microscopic surface model are given in the following sections.

2.1. Gas phase model

Continuum mass, energy and momentum balances allow for the modeling of the gas phase under the assumption of axisymmetric flow. The governing equations have been developed at length for CVD-type applications (e.g., (Vlachos, 1997; Lam and Vlachos, 2001; Christofides and Armaou, 2006)); however, here we apply the formulation by Armaou and Christofides (1999) as radial dependence of species concentration is desired.

Specifically, the mathematical model of the PECVD reactor consists of a particle velocity profile and four nonlinear dynamic diffusion–convection-reaction equations in two (radial and axial) dimensions (a set of four coupled parabolic PDEs). Specifically, by treating the gas phase as a three-dimensional stagnation flow, the evolution of the velocity profile within the PECVD reactor is computed from the Navier–Stokes and continuity equations. The spatio-temporal evolution of the concentration of the species, SiH_4, SiH_2, SiH_3 and H, throughout the reactor is obtained by applying dynamic material balances to the gas-phase and accounting for diffusive and convective mass transfer, and bulk and surface reactions. Finite-difference methods are then applied in order to discretize the spatial derivative of the species concentration in the r and z directions (z is defined as the direction normal to the wafer surface; see Fig. 1). Finally, time integration of the resulting ordinary differential equations is performed using the alternate direction implicit (ADI) method. More details on the model structure can be found in Armaou and Christofides (1999), and calculated steady-state concentration profiles are discussed further in the open-loop results section.

2.2. Surface microstructure model

Although kMC methodologies are commonly applied to the modeling of the growth of thin films, minor discrepancies in the physical phenomena included in the model can yield significantly different results. As such, the surface microstructure model is presented here in great detail, starting with the chemical model which acts as the foundation for the developing algorithm.

2.2.1. Two species thin film growth

To model the thin film surface growth, the following reaction scheme, which has been proposed and verified experimentally by Perrin et al. (1998) and Robertson (2000), and is shown schematically in Fig. 2, is adopted. Specifically, at standard operating conditions ($T < 300\ ^\circ C$) two species, SiH_3 and H, dominate the interactions on the growing film; therefore, all other species are ignored in the microscopic model. SiH_3 and H radicals reaching the film surface become physisorbed at hydrogenated silicon sites according to the following reactions:

$$\begin{aligned} SiH_3(g) + \equiv Si-H &\rightarrow \equiv Si-H\cdots SiH_3(s) \\ H(g) + \equiv Si-H &\rightarrow \equiv Si-H\cdots H(s). \end{aligned} \quad (1)$$

Physisorbed radicals rapidly diffuse across the surface according to the following reactions:

$$\begin{aligned} \equiv Si-H\cdots SiH_3(s) + \equiv Si-H &\rightarrow \equiv Si-H + \equiv Si-H\cdots SiH_3(s) \\ \equiv Si-H\cdots H(s) + \equiv Si-H &\rightarrow \equiv Si-H + \equiv Si-H\cdots H(s), \end{aligned} \quad (2)$$

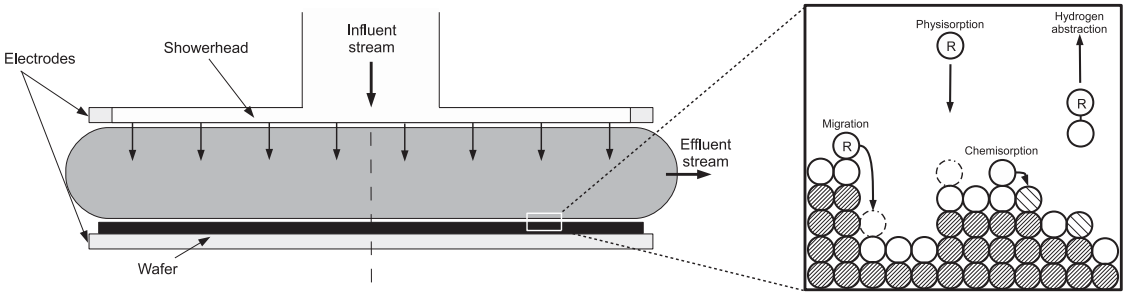

Fig. 1. Macroscopic (left) and microscopic (right) PECVD simulation regimes.

eventually contributing to one of two processes: hydrogen abstraction by a physisorbed SiH_3 radical forming SiH_4 and leaving behind a dangling bond according to the reaction:

$$\equiv Si-H\cdots SiH_3(s)+\equiv Si-H\cdots H(s)\rightarrow \equiv Si-H+\equiv Si^0+SiH_4(g), \quad (3)$$

or chemisorption at an existing dangling bond site according to the following reactions:

$$\equiv Si-H\cdots SiH_3(s)+\equiv Si^0\rightarrow \equiv Si-H+\equiv Si-SiH_3$$
$$\equiv Si-H\cdots H(s)+\equiv Si^0\rightarrow \equiv Si-H+\equiv Si-H. \quad (4)$$

Chemisorption of SiH_3 grows the height of a film site by one, whereas chemisorption of H returns the surface site to a hydrogenated state.

2.2.2. Lattice characterization

A one-dimensional solid-on-solid (SOS) lattice is used to model the thin film particle (each deposited species, SiH_3 or H, is modeled by a single particle) surface interactions via a hybrid kinetic Monte Carlo method which accounts for the four microscopic processes: physisorption, migration, hydrogen abstraction, and chemisorption.

The number of sites in the lateral direction is defined as the lattice size and denoted by L. Since a SOS lattice is used and the center of each particle is located on the lattice site, the heights of all sites are rounded to the nearest lattice site. The size of each lattice site is set to the diameter of a silicon atom ~ 0.25 nm, therefore the physical size of the lattice can be calculated by $0.25 \times L$. Particles are deposited with vertical incidence resulting in film growth normal to the lateral direction. The surface is roughened using 2400 randomly distributed deposition events to ensure that the initial configuration does not have a noticeable impact on the results. Periodic boundary conditions are applied at the edges of the lattice in the lateral direction.

As shown in Fig. 3(a), the top particle at any lattice position can exist in one of three states: a hydrogenated silicon atom available for physisorption, a radical currently physisorbed, or a dangling bond site available for chemisorption by migrating radicals. Physisorption and migration are hindered by currently occupied sites as each lattice position can take only a single state (i.e., sites containing physisorbed radicals are unavailable as deposition or migration destinations). Once chemisorbed, particles are fixed at that position, and in the case of silicon radicals the height of the lattice site grows by one. All other lattice particles are considered as bulk and their positions are permanently fixed. Hydrogen abstraction, shown in Fig. 3(a), cannot occur spontaneously, instead it requires the loss of a physisorbed radical. Although H and SiH_3 radicals both contribute to abstraction, in the present model only abstractions via SiH_3 radicals are considered due to the low operating temperatures ($< 350\ ^\circ C$) (Perrin et al., 1998).

The procedure for particle incorporation into the growing lattice can be seen in Fig. 3(b). A gas phase particle becomes physisorbed by vertical deposition on a hydrogenated surface site. The physisorbed radical rapidly migrates across the hydrogenated surface layer until encountering a dangling bond site. Chemisorption occurs instantaneously, and in the case of an SiH_3 radical shown here, growth of the lattice occurs and the surface site is returned to a hydrogenated state. Events are chosen randomly based on the relative rates of the microscopic phenomena described below.

2.2.3. Relative rates formulation

The surface kinetics presented below follow closely that of Tsalikis et al. (2013). Athermal or barrierless reactions involving gas phase species (e.g., physisorption) are evaluated using the fundamental kinetic theory of gases yielding the following rate equation:

$$r_a = J s_c N_a \sigma, \quad (5)$$

where J is the flux of gas-phase radicals, s_c is the local sticking coefficient, N_a is the Avogadro number, and σ is the average area per surface site. J can be calculated via the following equations:

$$J = \eta \bar{u}, \quad (6)$$

$$\eta = \frac{p_i}{RT}, \quad (7)$$

$$\bar{u} = \sqrt{\frac{8k_BT}{\pi m_i}}, \quad (8)$$

where η is the number density of radical i (here the reactive gas phase is assumed to be ideal), $\bar{u}$ is the mean radical velocity, p_i is the partial pressure of i, R is the gas constant, T is the temperature, k_B is the Boltzmann constant, and m is the molecular mass. Combining Eqs. (5)–(8) we obtain the overall reaction rate for an athermal radical i:

$$r_{a,i} = \frac{p_i}{RT}\sqrt{\frac{8k_BT}{\pi m_i}} s_c N_a \sigma. \quad (9)$$

Thermally activated kinetic events (e.g., migration and hydrogen abstraction) can be estimated using a standard Arehenius-type formulation:

$$r_{t,i} = \nu_i e^{-E_i/k_BT}, \quad (10)$$

where ν_i is the attempt frequency prefactor (s^{-1}) and E_i is the activation energy of radical i. Values for these parameters are drawn from Perrin et al. (1998) to correspond to the growth of a-Si:H films. Reaction mechanisms and resulting reaction rates for each kMC event are given in Table 1. Sticking coefficients are reported for athermal reactions as overall reaction rates depend on pressure and gas phase composition which typically vary. Thermally activated reaction rates are shown for $T = 500$ K to correspond to the operating temperature range used throughout this work.

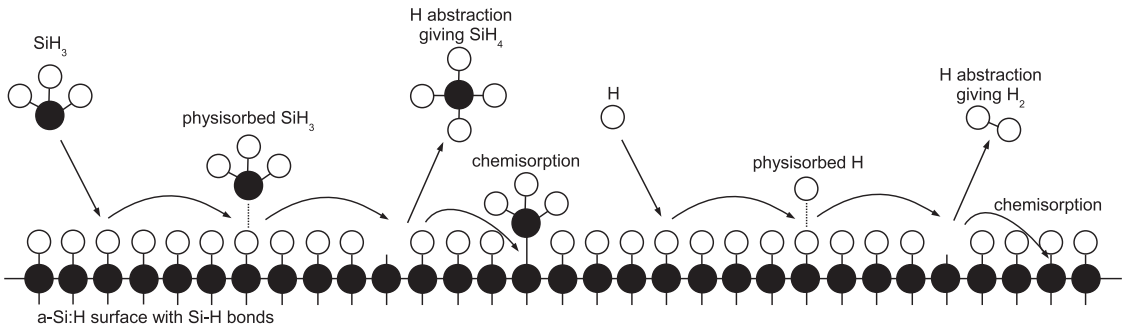

Fig. 2. Chemical model illustration showing particle–surface interactions.

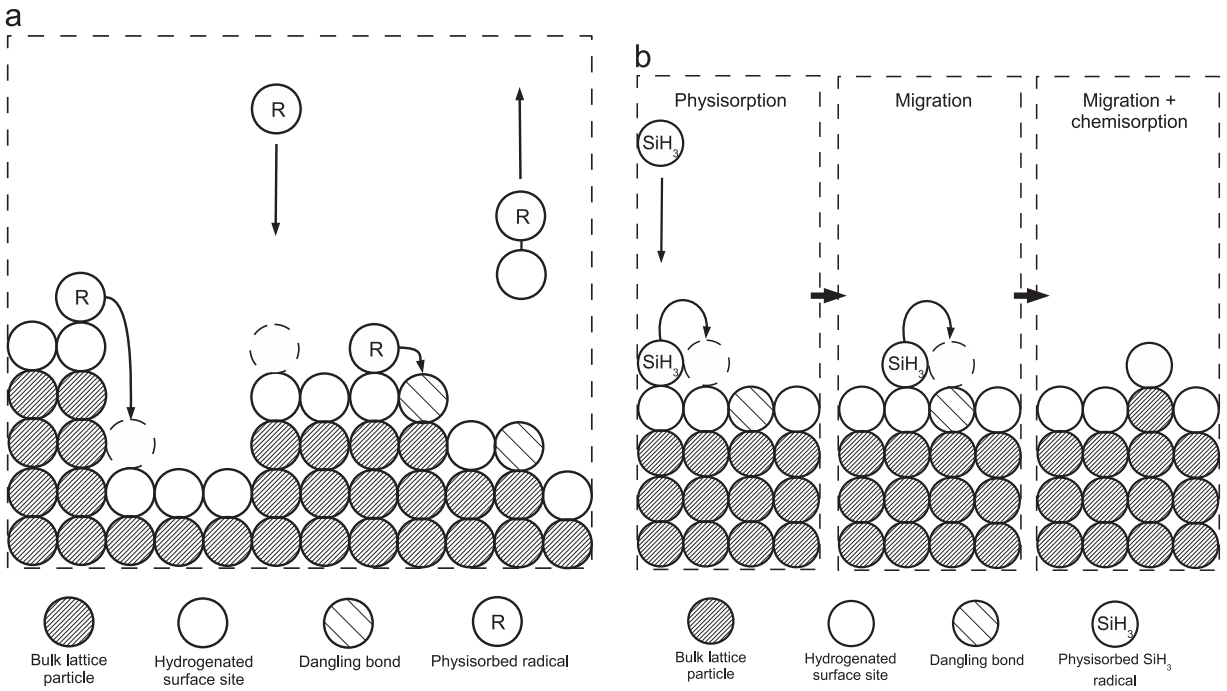

Fig. 3. Solid-on-solid lattice representation showing four microscopic processes. (a) Processes from left to right: physisorption, migration, chemisorption, and hydrogen abstraction. (b) Typical particle life cycle.

Table 1
Sticking coefficients and reaction rates composing the chemical model.

Thermally activated		Athermal reactions	
Reaction type	Reaction rate (s^{-1} $site^{-1}$)	Reaction type	Sticking coefficient
Hydrogen abstraction	3.35×10^5	SiH_3 physisorption	0.5
Hydrogen migration	1.58×10^{11}	Hydrogen physisorption	0.8
SiH_3 migration	1.16×10^{11}		

2.2.4. Kinetic Monte Carlo implementation

A standard n-fold kinetic Monte Carlo algorithm is applied to all events excluding migration which is handled using a one-dimensional lattice random walk process. The choice to exclude surface migration is made in the interest of computational efficiency and will be discussed in detail in the next subsection. The total reaction rate is defined as

$$r_{\text{total}} = r_a^H + r_a^{SiH_3} + r_t^{abs}, \tag{11}$$

where r_a^H is the rate of physisorption of hydrogen, r_t^{abs} is the rate of hydrogen abstraction, and $r_a^{SiH_3}$ is the rate of physisorption of SiH_3. A uniform random number, $(0, 1]$ is generated. If $\zeta_1 \le r_a^H / r_{\text{total}}$, then a hydrogen physisorption event is executed. If $r_a^H / R_{\text{total}} < \zeta_1 \le (r_a^H + r_t^{abs})/r_{\text{total}}$, then an abstraction event is executed. Finally, if $\zeta_1 > (r_a^H + r_t^{abs})/r_{\text{total}}$, then a silicon radical is physisorbed.

Physisorption proceeds by selecting a random lattice site from the available hydrogenated and dangling bond sites; if a dangling bond site is chosen, the radical is directly chemisorbed within the same kMC event. Otherwise, the radical is deposited onto the hydrogenated surface and execution continues. For the case of hydrogen abstraction, a random SiH_3 radical is chosen and removed. A dangling bond is created at the chosen site and kMC execution continues. Then, a second random number is drawn from a uniform distribution and the time increment for this kMC step is calculated by

$$\delta t = \frac{-\ln(\zeta_2)}{r_{\text{total}}}. \tag{12}$$

where $\zeta_1 \in (0, 1]$ is a uniform random number.

2.2.5. Decoupling surface migration

Due to the high frequency of surface migration events relative to physisorption or abstraction, a brute force kMC algorithm would expend $> 99\%$ of computation time on migration alone; see Fig. 4. At standard operating conditions, here $T = 500$ K, $P = 1$ Torr, and a gas phase SiH_3 mole fraction of 8.62×10^{-5}, it is clear that only a small fraction of computational time is spent on events contributing to reactions leading to film growth. Consequently, the simulation of surface particle migration is decoupled from our standard kMC implementation using a one-dimensional lattice random walk process.

As a result, we introduce a propagator to monitor the motion of physisorbed radicals. At the completion of each kMC cycle (a single physisorption or abstraction event), N_H hydrogen migration and N_{SiH_3} silane migration events are executed in succession, where N_H and N_{SiH_3} are defined as

$$N_H = \frac{r_t^H}{r_a^H + r_t^{abs} + r_a^{SiH_3}}, \quad N_{SiH_3} = \frac{r_t^{SiH_3}}{r_a^H + r_t^{abs} + r_a^{SiH_3}}, \tag{13}$$

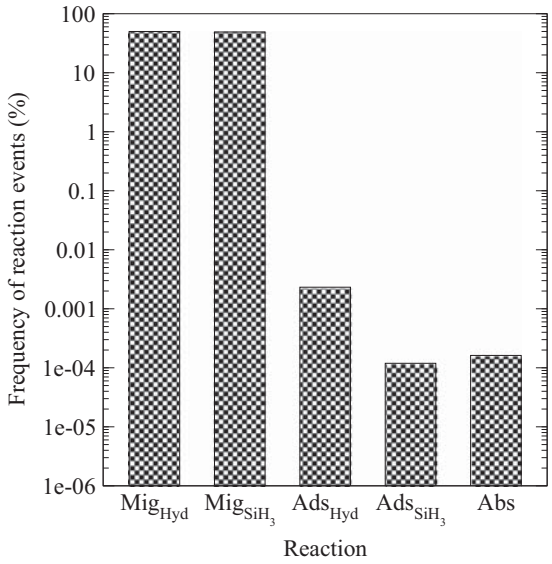

Fig. 4. Normalized frequency of reaction events within the present kMC scheme at $T=500$ K, $P=1$ Torr, and a SiH_3 mole fraction of 8.62×10^{-5}.

where r_t^H and $r_t^{SiH_3}$ are the thermally activated migration rates of hydrogen and silane radicals, respectively. N_H and N_{SiH_3} are split evenly among the n_H and n_{SiH_3} physisorbed radicals. A one-dimensional, weighted random walk process is then initiated whereby the bulk motion of a chosen radical is modeled by the propagator. Propagation steps are weighted such that an exponentially higher probability exists for a particle to relax down the lattice as opposed to jumping up lattice positions. After walking N/n steps, the final location of the propagator is stored as the radical's new position. This cycle is executed $n_H+n_{SiH_3}$ times, allowing each radical to migrate before the next kMC event is chosen. Similar to Eq. (12), the time increment for a single migration step is calculated via the following equations:

$$\delta t_H=\frac{-\ln(\zeta_i)}{r_t^H},\quad \delta t_{SiH_3}=\frac{-\ln(\zeta_i)}{r_t^{SiH_3}}. \tag{14}$$

Therefore, the total time required for all migration steps, Δt, is determined to be

$$\Delta t=\frac{-\ln(\zeta_i)}{r_t^H}\cdot N_H+\frac{-\ln(\zeta_i)}{r_t^{SiH_3}}\cdot N_{SiH_3}. \tag{15}$$

Film growth continues to develop in this fashion until the specified film thickness is reached.

We have validated our methodology for decoupling diffusive processes from the remaining kinetic events by confirming that the underlying lattice random walk process results: (a) in growth rates on par with experimental values, and (b) surface morphologies appropriate for given operating parameters.

3. Open-loop results

3.1. Growth rates and roughness

The fidelity of the hybrid kMC formulation to experimentally obtained film characteristics is determined using a flat, 100 particle length ($L=100$) lattice. The temperature, pressure, silane and hydrogen mole fractions are chosen as to represent industrially used PECVD parameters and to correspond to conditions for which reliable experimental data exist for the film growth rate and surface morphology.

Two pressure regimes are tested against the hybrid kMC model: low-pressure (<1 Torr), and high-pressure (≥1 Torr). Growth rates in the range of 1.3–5.5 Å/s have been reported by Lee et al. (1997) using substrate temperatures between 373 and 773 K in the low-pressure region. Although Lee et al. (1997) utilized an argon diluted feed stream, the inert gas is ignored here, and by replicating their reported pressure and silane concentration (400 mTorr and 20% SiH_4 gas), a simulated 100 nm thick lattice is grown at 5.4 Å/s at an operating temperature of 500 K. High deposition rates, ~12 Å/s, were achieved by Rech et al. (2001) and Perrin et al. (1998) using significantly higher operating pressures of 1–7 Torr. Our model exhibits a similar increase in growth rate within this region, with an average growth rate of 13.4 Å/s across 10 runs. These results are in good agreement with experimentally established growth rates in both the high and low pressure regimes. The morphology of the growing film must next be considered.

Here the root mean square (RMS) roughness is used in order to make a quantitative comparison of simulated flat films to reference films grown experimentally. RMS roughness is calculated via the following equation:

$$R_{rms}=\sqrt{\frac{1}{L}\sum_{i=1}^{L}\left(h_i-\overline{h}\right)^2}, \tag{16}$$

where h_i is the height of the lattice at position i and $\overline{h}$ is the mean height of the lattice. It is important to note here that for flat (i.e., ungrated) thin films the height and thickness of the lattice are equivalent terms ($h_i=\tau_i$). However, this is not true for thin films that utilize grated wafer substrates; in this case the height is defined as the total of the thin film thickness and the grating height at a given lattice site (i.e., $h_i=\tau_i+H_i$) (see, Fig. 8).

Using scanning tunneling microscopy, Tanenbaum et al. (1997) accurately measured the surface morphology during the evolution of a 50 nm thick amorphous silicon film deposited at 523 K and 540 mTorr. Mirroring these process parameters, a 100 particle lattice is grown and the rms roughness sampled at 1, 5, 10, 20, 40, and 50 nm thickness. Fig. 5 shows the evolution of surface roughness at each thickness. As represented by Fig. 6, the results match closely those reported by Tanenbaum et al. (1997), owing further confidence to the hybrid kMC methodology utilized here.

The above results indicate that microscopic growth can only produce surface texture on the order of a few nanometers. However, the diffusive transmittance of light has been characterized by Isabella et al. (2010a) to be dependent on roughness at significantly larger length scales. First, scattering can be enhanced using coarse grating where the geometrical dimensions of the rough surface are larger than the wavelength of light. Additionally, a second scattering mechanism becomes dominant when the vertical dimensions of the surface roughness become comparable

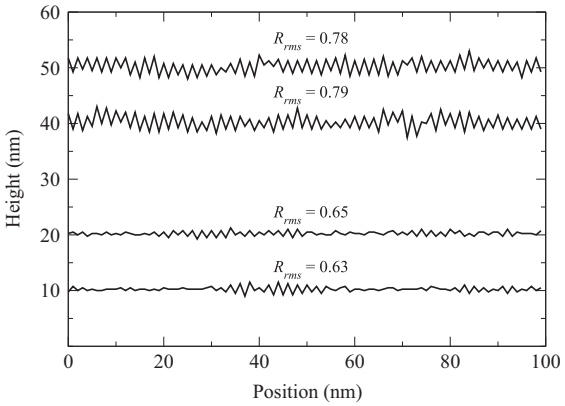

Fig. 5. Evolution of surface roughness during the growth of an $L=100$ flat film up to a thickness of $\overline{\tau}=50$ nm. Surfaces at 1 and 5 nm have been omitted for clarity.

to the wavelength of light. As a result, in an effort to increase light scattering and to obtain photocurrents from *a*-Si:H solar cells competitive with other existing solar cell technologies, surface roughness and height–height correlation length on the order of several hundred nanometers is desired (Eisele et al., 2001; Heine and Rudolf, 1995; Zeng et al., 2008; Sai et al., 2008; Campa et al., 2010; Isabella et al., 2010a,b; Li et al., 2011). Here we introduce grating to the wafer surface in order to impart a periodic texture that has been optimized for light trapping. A sinusoidal grated wafer is used to initialize the deposition lattice and the initial heights of all particles are calculated as follows:

$$h_0(x) = \frac{H}{2}[\cos(2\pi x/P) + 1], \quad x \in [0, L) \tag{17}$$

where H is the peak-to-peak amplitude or height of the lattice and P is the period. In this work, L, H, and P are all set to 1200 in order to yield an initial grating with a period and height of 300 nm as specified for optimal absorbance (Campa et al., 2010).

3.2. Film surface morphology at light wavelength scale

Given that the migration of physisorbed radicals constitutes the vast majority of surface reactions, the shape of the wafer surface may be obscured after the deposition of the absorbing thin film layer. A full period (L=1200) grated wafer is used here to determine the retention of initial grating shape parameters (i.e., height and period) after the growth of a 300 nm thick thin film. Fig. 7(a) shows the final film surface dimensions. The sinusoidal shape imparted by the grated wafer is retained after thin film growth. As can be seen from the overlay of the film surface onto the initial grating, Fig. 7(b), apart from local roughness on the order of nanometers, the wafer grating dimensions are preserved. The reason for this consistency can be attributed to the dangling bond growth mechanism: unlike traditional solid-on-solid kMC schemes, here particles migrating down the lattice cannot directly contribute to film growth without chemisorbing at an existing dangling bond site. This reinforces the importance of hydrogen abstraction to the growth rate of *a*-Si:H thin films, and eliminates the need for microscopic control of surface morphology.

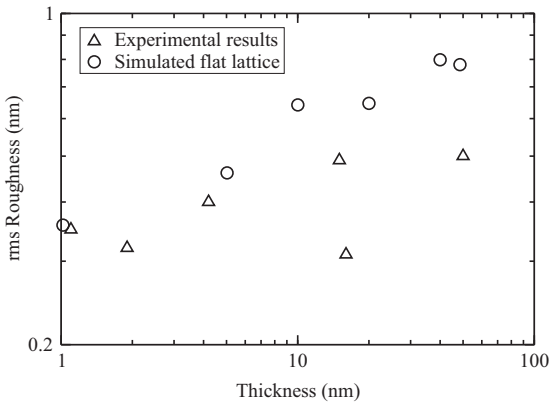

Fig. 6. Comparison of experimental and simulated RMS roughness at various film thicknesses.

3.3. Film thickness non-uniformity

Four parameters define the final shape of textured thin films: surface pattern, height H, period P, and film thickness τ. It has been shown that H and P are preserved from the initial grating, in this section, the proposed hybrid kMC model is applied at distinct locations across the wafer in order to investigate non-uniformity in film thickness due to the consumption of reactants across the wafer surface. As previously discussed, a steady-state concentration gradient for SiH_3 above the wafer surface has been calculated by Armaou and Christofides (1999) using finite-difference methods. A radial non-uniformity $> 17\%$ in the concentration of SiH_3 is observed from the center to the edge of the wafer. Here four zones are defined radially across the wafer surface and within each zone a single lattice period (L=1200) is simulated (see Fig. 8). An SiH_3 mole fraction of $x_{SiH_3} = 8.62 \times 10^{-5}$ in the first zone and mole fractions of 8.35, 7.86, and 7.25×10^{-5} in zones 2–4, respectively, are used to match the concentration profile adopted from Armaou and Christofides (1999). Identical sinusoidal grating is applied to each lattice with a height and period of 300 nm. The temperature of each zone is maintained at 500 K in a high-pressure region of 1 Torr. Experimental results suggest that an absorbing layer thickness of 300 nm be used for optimal light trapping in *a*-Si:H thin films (Zeman et al., 1997). Simulations using $x_{SiH_3} = 7.25 \times 10^{-5}$

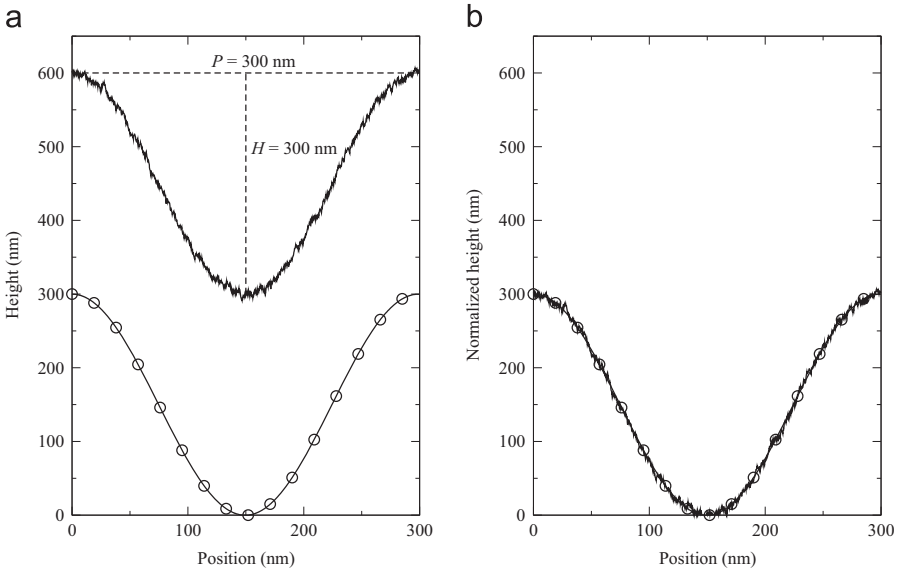

Fig. 7. Preservation of grating shape after the growth of a 300 nm thick *a*-Si:H thin film. (a) The grated wafer (bottom curve in left plot) at H and P=300 nm, with $\bar{\tau} = 300$ nm final film deposited above (top curve in left plot). (b) Thin film surface overlayed on the initial grating showing retention of desired sinusoidal shape. Note: Circles have been added to the grating profile for clarity.

(the mole fraction of zone 4) show an average deposition time of 246.996 s is required to reach this thickness set-point ($\bar{\tau} = 300$ nm). Therefore, each reactor zone is allowed to run for 246.996 s of physical growth (i.e., t=246.996 is deposition time not computational time). Open-loop simulation results are shown in Figs. 9–11.

As evidenced by Figs. 9 and 10, a 17% difference in SiH_3 concentration yields a 15% difference in film thickness from the center (r=0 cm) to the edge of the wafer (r=10 cm). The hydrogen abstraction event frequency (f_a) and RMS roughness of each zone remained relatively unchanged (Table 2, Fig. 11) ($a < 2$ nm increase in RMS roughness is negligible relative to the scale of visible light wavelengths). However, a marked decrease in event frequency from 3.36% to 2.85% for physisorption of SiH_3 (f_{SiH_3}) and increase from 63.31% to 63.81% for H (f_H) are present, as shown in Table 2. This result is expected due to the loss of SiH_3 radicals in the plasma phase as the process gas molecules travel across the wafer. An increased concentration of physisorbed SiH_3 relative to H near the center of the wafer allows for more rapid thin film growth as existing dangling bonds are more readily filled by migrating SiH_3 radicals. This effect can be overcome by either modulating the concentration of silane gas above the wafer using a closed-loop showerhead arrangement, or as proposed here, by utilizing radially spaced heating elements that allow for independently controlled substrate temperature zones.

4. Regulation of film thickness

A resulting non-uniformity in final film thickness of ~15% suggests the implementation of an operation strategy on the PECVD process to improve uniformity at the wafer scale. An increased concentration of physisorbed SiH_3 relative to H near the center of the wafer allows for more rapid film growth as existing dangling bonds are more readily filled by migrating SiH_3

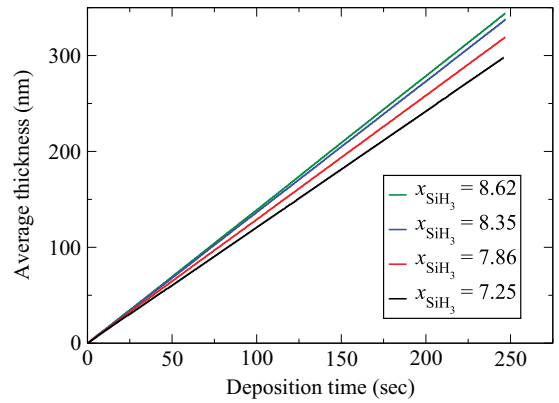

Fig. 10. Evolution of the thickness (nm) of the four radial wafer zones over time. Note: zone mole fractions are shown × 10^5.

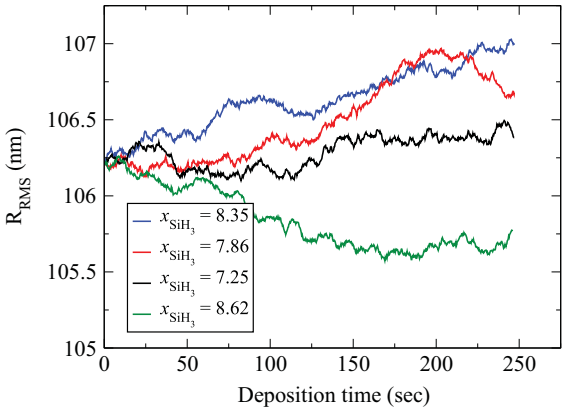

Fig. 11. Evolution of the RMS roughness of the four radial wafer zones over time. Note: zone mole fractions are shown × 10^5.

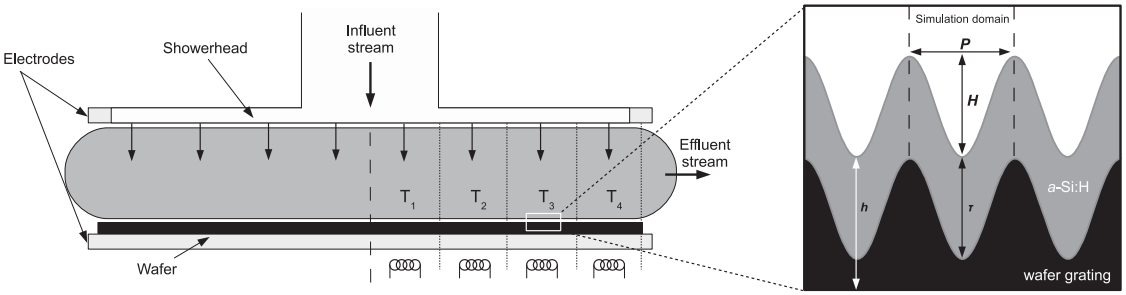

Fig. 8. Left: PECVD reactor showing four independent, concentric substrate temperature control zones. Right: microscopic simulation domain for a single grating period.

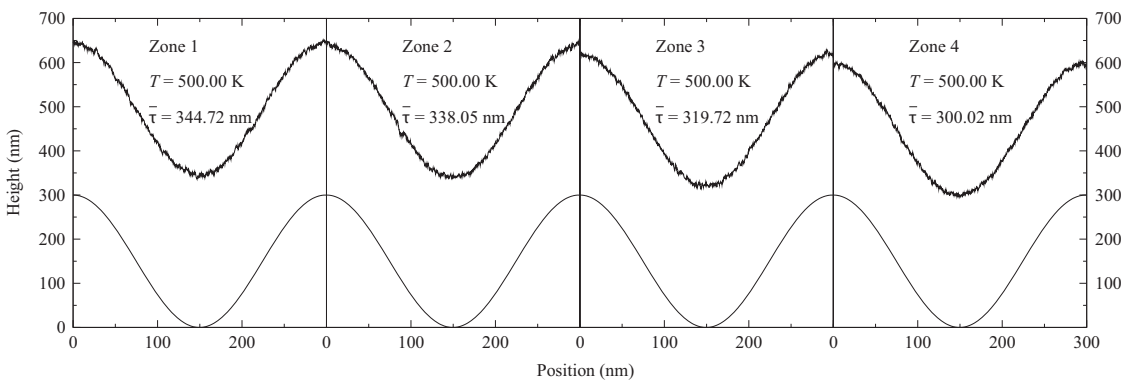

Fig. 9. Open-loop growth of sinusoidally grated thin films at 500 K and 1 Torr. From left to right: $x_{SiH_3} = 8.62$, 8.35, 7.86, and 7.25 × 10^{-5}, respectively. Note: Lattices are shown side by side for clarity, physical zones are composed of ~8 × 10^4 periods.

Table 2
Quantitative non-uniformity of four radial wafer zones.

Zone	f_{SiH_3}	f_H	f_a	R_{RMS}	$\bar{\tau}$ (nm)
1	3.36	63.31	33.33	106.38	344.72
2	3.26	63.41	33.33	106.68	338.05
3	3.07	63.59	33.33	107.00	319.72
4	2.85	63.81	33.33	105.77	300.02

Note: Frequencies are expressed as a percentage of total events excluding migration.

radicals. This effect can be overcome by either regulating the inlet concentration of silane gas above the wafer using a controlled showerhead arrangement (Armaou and Christofides, 1999), or, as proposed in this paper, by modulating the substrate temperature. Here four zones are defined radially across the wafer surface (Fig. 8) that allow for spatial manipulation of the substrate temperature. Due to the exponential dependence of hydrogen abstraction on surface temperature, the temperature set-point for each zone can be calculated a priori in order to overcome the SiH_3 concentration gap by increasing the fractional coverage of dangling bonds. Substrate temperature calculations are made using growth rate relations developed in the next section.

4.1. Growth rate relations

The relationship between substrate temperature (K), gas-phase mole fraction of SiH_3 (mol $\times 10^5$), and the thin film growth rate (Å/s) is shown in Fig. 12. Each data point represents the average growth rate across 10 runs of a sinusoidal lattice at $p=1$ Torr. (Note: error bars have been omitted due to relatively small deviations and for clarity.) Above 500 K growth is substantially slowed due to the inverse root dependence of SiH_3 physisorption on gas-phase temperature (see Eq. (9)). To avoid this plateau in growth, reactor operation is restricted to the region $\lesssim 500$ K.

As previously discussed, a steady-state concentration gradient for SiH_3 exists above the wafer surface with expected gas-phase concentrations of $x_{SiH_3}=8.62$, 8.35, 7.86, and 7.25×10^{-5} for substrate zones 1–4, respectively. By fixing the gas-phase composition at these values with a pressure of $p=1$ Torr, film growth is observed to be roughly linear with respect to substrate temperature (Fig. 13 shows this relationship for the gas-phase mole fractions of SiH_3 in zones 1–3). As a result, the following linear growth rate equations can be fit using standard least squares methods:

$$G(T)=0.238T-105.274\ \text{Å K}^{-1}\ \text{s}^{-1},\quad x_{SiH_3}=8.62$$
$$G(T)=0.254T-113.673\ \text{Å K}^{-1}\ \text{s}^{-1},\quad x_{SiH_3}=8.35$$
$$G(T)=0.227T-100.875\ \text{Å K}^{-1}\ \text{s}^{-1},\quad x_{SiH_3}=7.86 \qquad (18)$$

4.2. Regulating substrate temperature

The pressure within each zone is maintained at $p=1$ Torr. Zone 4, the zone with the slowest relative growth, is used as a reference and hence the parameters remain fixed ($x_{SiH_3}=7.25$ and $T=500$ K). The mole fractions of zones 1–3 are set as described previously to 8.62, 8.35, and 7.86×10^{-5}, respectively. The necessary temperature set-point for each zone is calculated via Eq. (18) such that all growth rates match that of zone 4. (Note: zone 4 is chosen as a reference point in order to avoid operating the reactor above 500 K.) The simulation parameters are summarized in Table 3.

Fig. 14 shows the film surface profile for each zone after $t=246.996$ s of growth (the time required for zone 4 to reach $\bar{\tau}=300$ nm). Event frequency and thin film thickness data have been summarized in Table 4. A difference of $\sim0.68\%$ exists in the thickness of the *a*-Si:H thin film across the wafer. As discussed previously, the frequency of physisorption of SiH_3 shows a significant decrease toward the edge of the wafer due to the consumption of process gas. Although a greater number of SiH_3 radicals are present on the surface of the growing film, a decreased density of dangling bonds (due to a lower frequency of hydrogen abstraction f_a) in the inner zones allows for significant reduction in thin film thickness non-uniformity relative to deposition at a spatially uniform substrate temperature.

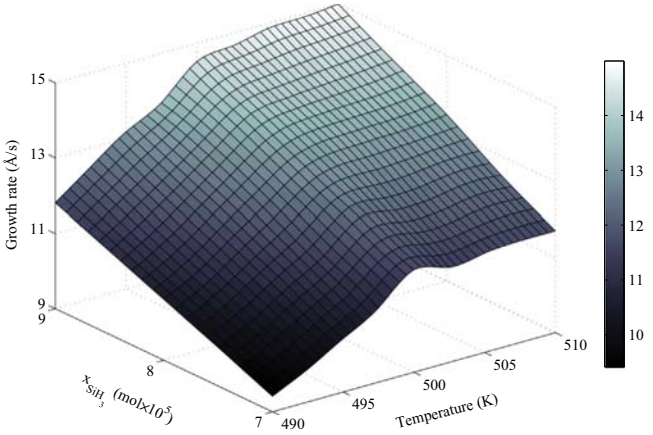

Fig. 12. Relationship between growth rate, substrate temperature, and gas-phase mole fraction of SiH_3. Mole fractions, x_{SiH_3}, are shown $\times 10^5$.

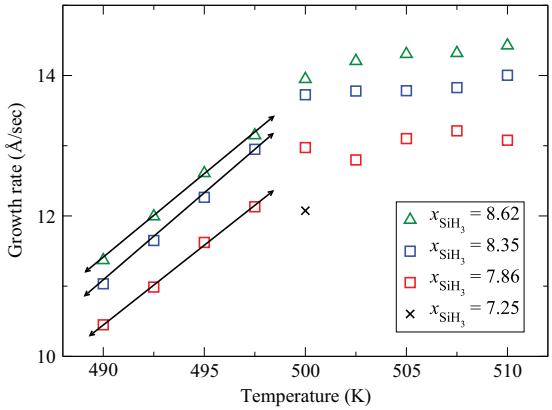

Fig. 13. Linear relationships between growth rate and temperature for each reactor zone. Mole fractions, x_{SiH_3}, are shown $\times 10^5$. A single data point exists for $x_{SiH_3}=7.25$ as zone 4 remains a fixed reference.

Table 3
Calculated operating parameters by zone.

Zone	x_{SiH_3} ($\times 10^{-5}$)	p (Torr)	T (K)
1	8.62	1	493.06
2	8.35	1	495.07
3	7.86	1	497.58
4	7.25	1	500.00

4.3. Roughness dependence on substrate temperature variation

Regulation of the surface temperature may affect the roughness (R_{RMS}) leading to further non-uniformity between reactor zones. Here we simulate the growth of 300 nm thick thin film with sinusoidal grating at $p=1$ Torr. The temperature is varied from 490

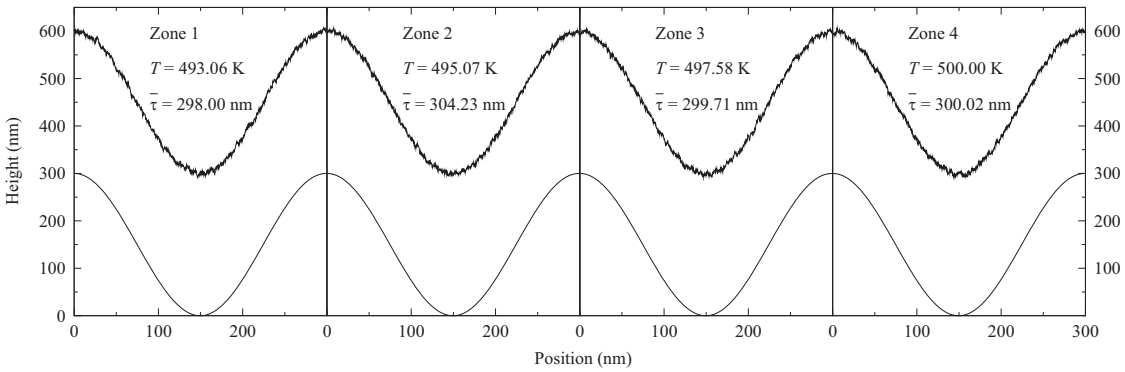

Fig. 14. Surface microstructure and thickness of sinusoidally grated thin films with spatially dependent temperatures. From left to right: $x_{SiH_3} = 8.62$, 8.35, 7.86, and 7.25×10^{-5}, respectively. Note: lattices are shown side by side for clarity, physical zones are composed of $\sim 8 \times 10^4$ periods.

Table 4
Quantitative non-uniformity of four radial wafer zones.

Zone	f_{SiH_3}	f_H	f_a	R_{RMS}	$\bar{\tau}$ (nm)
1	3.35	63.32	33.33	106.82	298.00
2	3.25	63.41	33.33	106.50	304.23
3	3.07	63.60	33.33	106.14	299.71
4	2.85	63.82	33.33	105.77	300.02

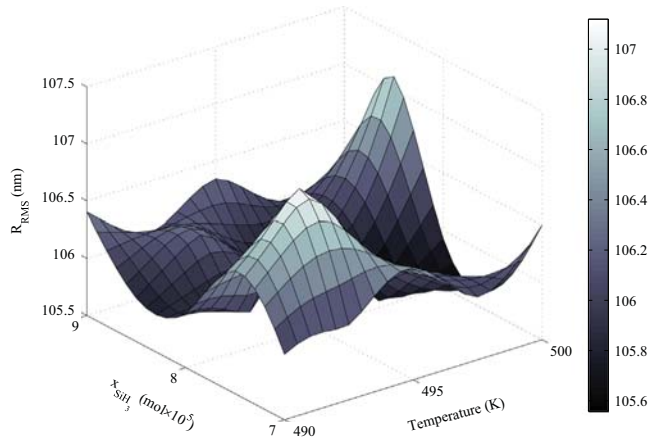

Fig. 15. Relationship between surface roughness, substrate temperature, and gas-phase mole fraction of SiH_3. Mole fractions, x_{SiH_3}, are shown $\times 10^5$.

to 500 K and the mole fraction of SiH_3 in the gas-phase is varied from 7 to 9×10^{-5}. The relationship between substrate temperature (K), gas-phase mole fraction of SiH_3 (mol $\times 10^5$), and the surface roughness (R_{RMS}, nm) is shown in Fig. 15. Each data point represents the average roughness across 10 runs of a sinusoidal lattice at $p = 1$ Torr. (Note: Error bars have been omitted due to relatively small deviations and for clarity.)

A slight trend of increasing roughness is shown to occur at low substrate temperatures and low gas-phase mole fractions of SiH_3 (Fig. 15). At low substrate temperatures the frequency of hydrogen physisorption is far greater than that of SiH_3 physisorption and hydrogen abstraction, as evidenced by Eqs. (9) and (10). As a result, the mobility of SiH_3 radicals is hindered which increases the roughness of the growing film surface. Additionally, at high SiH_3 gas-phase concentrations, SiH_3 radicals more readily physisorb at hydrogenated surface sites, effectively lowering the fractional coverage of hydrogen radicals and the observed surface roughness. A slight decrease in surface roughness is observed from zone 1 (which operates at $T = 493$ K and $x_{SiH_3} = 8.62 \times 10^{-5}$) to zone 4 (which operates at $T = 500$ K and $x_{SiH_3} = 7.25 \times 10^{-5}$) which may be attributed to the combined effect of the simultaneous increase in substrate temperature and decrease in SiH_3 mole fraction; evidence of this observed behavior is shown in Table 4. However, as discussed in previous sections, fluctuations in the surface roughness on the order of a few nanometers will not affect light trapping which occurs at the scale of visible light wavelengths.

4.4. Robustness to model uncertainty

Uncertainties in radio frequency and heating element power may cause stochastic variation in process parameters that lead to increased non-uniformity in final film thickness. The robustness of our multiscale model to these fluctuations is explored using independent variation of the concentration of SiH_3 radicals, x_{SiH_3}, and the surface temperature, T, as well as concurrent variations in these parameters.

First, the necessary temperatures for zones 1–4 remain fixed at the values calculated previously to reduce radial thickness non-uniformity. In a similar manner to the previous section, the pressure within each zone is maintained at $p = 1$ Torr and zone 4, the outermost zone, is used as a reference and hence the simulation is terminated once 246.996 s of deposition time (the average time required for zone 4 to reach a thickness of 300 nm at $T = 500$ K and $x_{SiH_3} = 7.25 \times 10^{-5}$) has elapsed. However, the concentration of radicals is allowed to vary by 1% above and below the expected values proposed by Armaou and Christofides (1999) to account for uncertainties in RF power. For each simulation a sinusoidally grated thin film with height H and period $P = 300$ nm is used. Operating parameters and resulting film thicknesses for independent variations are shown at the top of Table 5. (Note: values represent the maximum non-uniformity achieved within the allowed 1% fluctuation.)

As expected, while maintaining the optimal temperature profile calculated previously, variations in gas-phase SiH_3 radical concentration increase final film thickness non-uniformity;

Table 5
Final film thickness for sinusoidally grated thin films in the presence of independent variations in x_{SiH_3} and T.

Variable	Zone	x_{SiH_3} ($\times 10^{-5}$)	T (K)	$\bar{\tau}$ (nm)
x_{SiH_3}	1	8.53	493.06	297.41
	2	8.43	495.07	306.11
	3	7.78	497.58	297.17
	4	7.32	500.00	303.25
T	1	8.62	492.56	292.39
	2	8.35	495.57	307.32
	3	7.86	498.08	303.00
	4	7.25	500.50	299.75

Table 6
Final thin film thickness for sinusoidally grated wafers in the presence of concurrent variations in x_{SiH_3} and T.

Variable	Zone	x_{SiH_3} ($\times 10^{-5}$)	T (°C)	$\bar{\tau}$ (nm)
x_{SiH_3}, T	1	8.53	492.56	291.13
	2	8.43	495.57	309.67
	3	7.78	498.08	299.04
	4	7.32	500.50	301.85

however, the difference of 2.9% in the thickness of zones 2 and 3 remains relatively close to that of the initial optimized case (1.5%).

Second, the concentration of each zone is returned to the steady-state concentration gradient while the temperature is allowed to fluctuate within 0.5 K above and below the target values calculated previously using the proposed linear growth rate relations. Again, for each simulation a sinusoidally grated thin film with height H and period $P=300$ nm is used. Operating parameters and resulting final film thicknesses for independent variations are shown at the bottom of Table 5. (Note: table values represent the maximum non-uniformity achieved within the allowed 0.5 K fluctuation.)

A difference of 4.8% exists between the thickness of the zones 1 and 2. This result is expected given the linear relationship between film growth rate and surface temperature developed in previous sections. Although a 4.8% non-uniformity in thickness is significantly higher than the 0.68% non-uniformity reported for the optimal case, great improvement is still shown over the 15% non-uniformity experienced before substrate temperature regulation.

Finally, stochastic variations in the RF and heating element power are considered in tandem to account for concurrent uncertainties that may occur during operation. Independent fluctuations in SiH_3 concentration and substrate temperature that lead to maximum thickness non-uniformity are also applied here. Operating parameters and final film thicknesses are shown in Table 6.

Owing to contributions from both fluctuation sources, SiH_3 concentration and substrate temperature, a final film thickness non-uniformity of 6.0% is present. Again, this is a non-negligible difference in film thickness across the wafer; however, this represents the maximum non-uniformity experienced within the allowed parameter fluctuations, and a significant reduction from the initial 15% non-uniformity, validating the multiscale modeling and control strategy proposed in this work.

5. Conclusions

The present work focuses on the development of a multiscale modeling and operation framework for PECVD of thin film silicon solar cells with uniform thickness and film surface microstructure that optimizes light trapping. The macroscopic model of the gas phase is based on the hypothesis of continuum and provides the deposition rate profile across the wafer. The proposed microscopic model which utilizes a hybrid kinetic Monte Carlo algorithm that accounts for interactions amongst physisorbed radicals, chemisorption, and hydrogen abstraction, has been shown to reproduce experimentally obtained surface morphologies and growth rates. Initial simulations using flat lattices have shown that roughness is limited to a few nanometers and validated the need for grated wafer substrates in order to achieve roughness and height–height correlation length on the order of visible light wavelengths. The sinusoidal shape of grated wafers with a height and period of 300 nm has been shown to be preserved after the growth of amorphous silicon thin films up to 300 nm thickness. The retention of grating shape is attributed to the dependence of film growth on hydrogen abstraction, eliminating the need for microscale control of surface morphology. However, radially non-uniform deposition rates of the film on the wafer owing to gas-phase transport phenomena have shown that a 17% difference in SiH_3 concentration can yield a 15% difference in film thickness from the center ($r=0$ cm) to the edge of the wafer ($r=10$ cm). Due to the observed dependence of film growth rate on substrate temperature, the wafer surface has been separated into four concentric zones, each with an independent heating element. Extensive simulations demonstrate that the use of appropriate sinusoidal wafer grating and the regulation of substrate temperature provide a viable and effective way for the PECVD of thin film silicon solar cells with uniform thickness ($<1\%$) and film surface microstructure that optimizes light trapping, and were found to be robust with respect to model uncertainty.

Acknowledgments

Financial support from the National Science Foundation (NSF), CBET-1262812, is gratefully acknowledged.

References

Armaou, A., Christofides, P.D., 1999. Plasma enhanced chemical vapor deposition: modeling and control. Chem. Eng. Sci. 54, 3305–3314.
Campa, A., Isabella, O., Erven, R., Peeters, P., Borg, H., Krc, J., Topic, M., Zeman, M., 2010. Optimal design of periodic surface texture for thin-film a-Si:H solar cells. Prog. Photovolt.: Res. Appl. 18, 160–167.
Christofides, P.D., Armaou, A., 2006. Control and optimization of multiscale process systems. Comput. Chem. Eng. 30, 1670–1686.
Eisele, C., Nebel, C.E., Stutzmann, M., 2001. Periodic light coupler gratings in amorphous thin film solar cells. J. Appl. Phys. 89, 7722–7726.
van Erven, A.J.M., Franken, R.H., Ruijter, J., Peeters, P., Vugts, W., Isabella, O., Zeman, M., Haase, C., 2008. Controlled texturing of thin film silicon solar cell substrates. In: Proceedings of 23rd European Photovoltaic Solar Energy Conference, Valencia, Spain.
Gallagher, A., 1988. Neutral radical deposition from silane discharges. J. Appl. Phys. 63, 2406–2413.
Geis, M., Flanders, D., Smith, H., 1979. Crystallographic orientation of silicon on an amorphous substrate using an artificial surface-relief grating and laser crystallization. Appl. Phys. Lett. 35, 71–74.
Green, M., Emery, K., Hishikawa, Y., Warta, W., Dunlop, E., 2014. Solar cell efficiency tables. Prog. Photovolt.: Res. Appl. 22, 701–710.
Heine, C., Rudolf, H., 1995. Submicrometer gratings for solar energy applications. Appl. Opt. 34, 2476–2482.
Huang, J., Orkoulas, G., Christofides, P.D., 2012a. Modeling and control of transparent conducting oxide layer surface morphology for improved light trapping. Chem. Eng. Sci. 74, 135–147.
Huang, J., Orkoulas, G., Christofides, P.D., 2012b. Surface morphology control of transparent conducting oxide layers for improved light trapping using wafer grating and feedback control. Chem. Eng. Sci. 81, 191–201.
Isabella, O., Krc, J., Zeman, M., 2010a. Modulated surface textures for enhanced light trapping in thin-film silicon solar cells. Appl. Phys. Lett. 97, 101106.
Isabella, O., Moll, F., Krc, J., Zeman, M., 2010b. Moldulated surface textures using zinc-oxide films for solar cells applications. Phys. Status Solidi 207, 642–646.
Kern, W., 1991. Thin Film Processes II. Academic Press.
Kreiger, M., Shonnard, D., Pearce, J., 2013. Life cycle analysis of silane recycling in amorphous silicon-based solar photovoltaic manufacturing. Resour. Conserv. Recycl. 70, 44–49.
Lam, R., Vlachos, D.G., 2001. Multiscale model for epitaxial growth of films: growth mode transition. Am. Phys. Soc. 64, 035401.
Lee, J., Choi, Y., Lee, B., Ahn, B., 1997. Microwave-induced low-temperature crystallization of amorphous silicon thin films. J. Appl. Phys. 82, 2918–2921.
Li, H., Wang, Q., Chen, J., Krc, J., Soppe, W.J., 2011. Light trapping in amorphous silicon solar cells with periodic grating structures. Opt. Commun. 285, 808–815.
Novikov, P., Donne, A., Cereda, S., Miglio, L., Pizzini, S., Binetti, S., Rondanini, M., Cavallotti, C., Chrastina, D., Moiseev, T., Kanel, H., Isella, G., Montalenti, F., 2009. Crystallinity and microstructure in Si films grown by plasma-enhanced chemical vapor deposition: a simple atomic-scale model validated by experiments. Appl. Phys. Lett. 94, 051904.
Pandey, S., Singh, T., Maroudas, D., 2009. Kinetic Monte Carlo simulations of surface growth during plasma deposition of silicon thin films. J. Chem. Phys. 131, 034503.

Perrin, J., Shiratani, M., Kae-Nune, P., Videlot, H., Jolly, J., Guillon, J., 1998. Surface reaction probabilities and kinetics of H, SiH_3, Si_2H_5, CH_3, and C_2H_5 during deposition of *a*-Si: H and *a*-C:H from H_2, SiH_4, and CH_4 discharges. J. Vac. Sci. Technol. A 16, 278–289.

Rech, B., Roschek, T., Muller, J., Wieder, S., Wagner, H., 2001. Amorphous and microcrystalline silicon solar cells prepared at high deposition rates using RF (13.56 MHz) plasma excitation frequencies. Sol. Energy Mater. Sol. Cells 66, 267–273.

Rech, B., Wagner, H., 1999. Potential of amorphous silicon for solar cells. Appl. Phys. A 69, 155–167.

Robertson, J., 2000. Deposition mechanism of hydrogenated amorphous silicon. J. Appl. Phys. 87, 2608–2617.

Sai, H., Fujiwara, H., Kondo, M., Kanamori, Y., 2008. Enhancement of light trapping in thin-film hydrogenated microcrystalline Si solar cells using back reflectors with self-ordered dimple pattern. Appl. Phys. Lett. 93, 143501.

Sansonnens, L., Bondkowski, J., Mousel, S., Schmitt, J., Cassagne, V., 2003. Development of a numerical simulation tool to study uniformity of large area PECVD film processing. Thin Solid Films 427, 21–26.

Stephan, U., Kuske, J., Gruger, H., Kottwitz, A., 1999. Problems of power feeding in large area PECVD of amorphous silicon. Mat. Res. Soc. Symp. Proc. 557, 157–162.

Tanenbaum, D., Laracuente, A., Gallagher, A., 1997. Surface roughening during plasma-enhanced chemical-vapor deposition of hydrogenated amorphous silicon on crystal silicon substrates. Phys. Rev. B 56, 4243–4250.

Tsalikis, D., Baig, C., Mavrantzas, V., Amanatides, E., Mataras, D., 2013. A hybrid kinetic Monte Carlo method for simulating silicon films grown by plasma-enhanced chemical vapor deposition. J. Chem. Phys. 139, 204706.

Vlachos, D.G., 1997. Multiscale integration hybrid algorithms for homogeneous–heterogeneous reactors. AIChE J. 43, 3031–3041.

Yang, C., Smith, L., Arthur, C., Parsons, G., 2000. Stability of low-temperature amorphous silicon thin film transistors formed on glass and transparent plastic substrates. J. Vac. Sci. Technol. B 18, 683–689.

Zeman, M., Willemen, J., Vosteen, L., Tao, G., Metselaar, J., 1997. Silicon modelling of current matching in *a*-Si: H/*a*-Si:H tandem solar cells on textured TCO substrates. Sol. Energy Mater. Sol. Cells 46, 81–99.

Zeng, L., Bermel, P., Yi, Y., Alamariu, B., Broderick, K., Liu, J., Hong, C., Duan, X., Joannopoulos, J., Kimberling, L., 2008. Demonstration of enhanced absorption in thin film Si solar cells with textured photonic crystal back reflector. Appl. Phys. Lett. 93, 221105.